2019-12

SENSIBLE AND LATENT HEAT FLUXES ACROSS THE MARGINAL ICE ZONE AND IRMINGER CURRENT

Wells, Benjamin B.

Monterey, CA; Naval Postgraduate School

NAVAL POSTGRADUATE SCHOOL

MONTEREY, CALIFORNIA

THESIS

SENSIBLE AND LATENT HEAT FLUXES ACROSS THE MARGINAL ICE ZONE AND IRMINGER CURRENT

by

Benjamin B. Wells

December 2019

Thesis Advisor: Haflidi H. Jonsson
Co-Advisor: Scott Powell

THIS PAGE INTENTIONALLY LEFT BLANK

REPORT DOCUMENTATION PAGE	*Form Approved OMB No. 0704-0188*

1. AGENCY USE ONLY *(Leave blank)*	**2. REPORT DATE** December 2019	**3. REPORT TYPE AND DATES COVERED** Master's thesis

4. TITLE AND SUBTITLE
SENSIBLE AND LATENT HEAT FLUXES ACROSS THE MARGINAL ICE ZONE AND IRMINGER CURRENT

5. FUNDING NUMBERS

6. AUTHOR(S) Benjamin B. Wells

7. PERFORMING ORGANIZATION NAME(S) AND ADDRESS(ES)
Naval Postgraduate School
Monterey, CA 93943-5000

8. PERFORMING ORGANIZATION REPORT NUMBER

9. SPONSORING / MONITORING AGENCY NAME(S) AND ADDRESS(ES)
N/A

10. SPONSORING / MONITORING AGENCY REPORT NUMBER

11. SUPPLEMENTARY NOTES The views expressed in this thesis are those of the author and do not reflect the official policy or position of the Department of Defense or the U.S. Government.

12a. DISTRIBUTION / AVAILABILITY STATEMENT
Approved for public release. Distribution is unlimited.

12b. DISTRIBUTION CODE
A

13. ABSTRACT (maximum 200 words)

Sensible and latent heat fluxes over the Marginal Ice Zone (MIZ) are an area of active research. Polar lows that develop near the MIZ have far-reaching impacts on shipping and personnel but are often misrepresented by models of the atmosphere. The accurate simulation of polar lows depends on adequate representation of energy transport between the atmosphere and ocean. Fluxes were explored with respect to ice concentration near the Irminger Current, located north of Iceland, with atmospheric measurements taken from the NPS Twin Otter aircraft. Because no widely accepted method exists for computing fluxes over a dynamic, ice-covered ocean surface that not only varies in surface roughness but also the damping effect of ice, a dynamic Charnock number that was dependent on ice concentration—in lieu of a constant Charnock number—was tested. However, ice concentration could not be derived using in situ atmospheric measurements or sea surface temperatures. Thousands of high-resolution photographs were taken of the surface from flight level, and a machine learning (ML) technique was applied to the photographs to efficiently identify ice and open water in order to estimate ice concentration.

14. SUBJECT TERMS aircraft, air-sea, heat fluxes, machine learning	**15. NUMBER OF PAGES** 67
	16. PRICE CODE

17. SECURITY CLASSIFICATION OF REPORT	**18. SECURITY CLASSIFICATION OF THIS PAGE**	**19. SECURITY CLASSIFICATION OF ABSTRACT**	**20. LIMITATION OF ABSTRACT**
Unclassified	Unclassified	Unclassified	UU

NSN 7540-01-280-5500 Standard Form 298 (Rev. 2-89)
Prescribed by ANSI Std. 239-18

THIS PAGE INTENTIONALLY LEFT BLANK

Approved for public release. Distribution is unlimited.

SENSIBLE AND LATENT HEAT FLUXES ACROSS THE MARGINAL ICE ZONE AND IRMINGER CURRENT

Benjamin B. Wells
Lieutenant Commander, United States Navy
BS, University of Northern Colorado, 2003

Submitted in partial fulfillment of the
requirements for the degree of

MASTER OF SCIENCE IN METEOROLOGY AND PHYSICAL OCEANOGRAPHY

from the

NAVAL POSTGRADUATE SCHOOL
December 2019

Approved by: Haflidi H. Jonsson
Advisor

Scott Powell
Co-Advisor

Wendell A. Nuss
Chair, Department of Meteorology

THIS PAGE INTENTIONALLY LEFT BLANK

ABSTRACT

Sensible and latent heat fluxes over the Marginal Ice Zone (MIZ) are an area of active research. Polar lows that develop near the MIZ have far-reaching impacts on shipping and personnel but are often misrepresented by models of the atmosphere. The accurate simulation of polar lows depends on adequate representation of energy transport between the atmosphere and ocean. Fluxes were explored with respect to ice concentration near the Irminger Current, located north of Iceland, with atmospheric measurements taken from the NPS Twin Otter aircraft. Because no widely accepted method exists for computing fluxes over a dynamic, ice-covered ocean surface that not only varies in surface roughness but also the damping effect of ice, a dynamic Charnock number that was dependent on ice concentration—in lieu of a constant Charnock number—was tested. However, ice concentration could not be derived using in situ atmospheric measurements or sea surface temperatures. Thousands of high-resolution photographs were taken of the surface from flight level, and a machine learning (ML) technique was applied to the photographs to efficiently identify ice and open water in order to estimate ice concentration.

THIS PAGE INTENTIONALLY LEFT BLANK

TABLE OF CONTENTS

THIS PAGE INTENTIONALLY LEFT BLANK

LIST OF FIGURES

LIST OF TABLES

THIS PAGE INTENTIONALLY LEFT BLANK

LIST OF ACRONYMS AND ABBREVIATIONS

ABL	Atmospheric Boundary Layer
AVHRR	Advanced Very High Resolution Radiometer
C_{DN}	Neutral Drag Coefficient
CRF	Conditional Random Field
DCNN	Deep Convolutional Neural Network
EGC	East Greenland Current
FN	Flight number
GFS	Global Forecast System
GPU	Graphical Processing unit
GT	Ground Truth
GUI	Graphical User Interface
Hz	Hertz (1/seconds)
IC	Irminger Current
IR	Infra-Red
LH	Latent Heat Flux
MIZ	Marginal Ice Zone
ML	Machine Learning
NPS	Naval Postgraduate School
PBL	Planetary Boundary Layer
PL	Polar Low
QC	Quality Control
SH	Sensible Heat Flux
SST	Sea Surface Temperature

THIS PAGE INTENTIONALLY LEFT BLANK

ACKNOWLEDGMENTS

Without the undying support of my amazing family, Tv, Brogan, and Beni, my life would not be complete and this would not be possible.

My parents, Benjamin and Sandy Wells, and Karie and Craig Brown have given me the moral compass and fortitude to accomplish many things in life and I can never thank them enough.

Dr. Haflidi Jonsson and Dr. Scott Powell have become more than advisors. They gave me exactly the right amount of encouragement, leeway, and direction to keep me both interested and motivated to accomplish this work.

CDR Paula Travis… We did it! Thank you!

THIS PAGE INTENTIONALLY LEFT BLANK

I. INTRODUCTION

The Marginal Ice Zone (MIZ) is defined by the National Ice Center as the transition zone between the open ocean (ice free) and pack ice (≥80% concentration) (U.S. National Ice Center, Naval Ice Center 2019). The dynamic oceanographic and atmospheric nature of the MIZ is difficult to accurately sense, describe, and integrate into models. While satellite measurements are plentiful from polar orbiting platforms, surface properties are often hidden under cloud cover, the width of the satellite footprint is small relative to the width of the MIZ, and the satellite's spatial resolution is not fine enough to pick out individual ice floats in the MIZ. The cost of placing high latitude surface sensors and rawinsonde sites in the MIZ can be prohibitive, winter weather is destructive and ocean currents can be strong; therefore, sensors placed in the MIZ are short lived and data are sparse. Sparsity of data hinders validation of satellite measurements, and thus degrades data used as initial conditions in models. In situ measurements and studies are needed to validate model parameterizations and verify the model output. Understanding the MIZ is also of increasing strategic, tactical, political, commercial, and scientific importance. With increasing ice-melt in the Arctic, previously closed shipping lanes are opening up along the MIZ, and harvesting oil and minerals from the sea bottom is becoming possible (U.S. Coast Guard 2013). This results in increasing political interest in the Arctic region and increased military activity.

The MIZ is a dynamic area that plays an important role in the Earths energy balance. Sudden unexpected and un-modeled polar lows (PL) that originate at the MIZ can be attributed to unresolved frontogenesis and cyclogenesis in this dynamic zone (Adakudlu 2011) (Pagowski et al. 2001). Ice cover acts as a barrier that prevents energy transfer to the atmosphere from the ocean. PLs propagating over areas where the ice has retreated will intensify (Sergeev 2018), causing high winds, seas, and cold air outbreaks further south. If these effects are not properly assimilated into models, forecasters may not be able to adequately warn vessels or populations of the effects of these storms.

The scarcity of data on surface conditions in the MIZ has recently inspired some attempts to use aircraft for such measurements. However, this is frequently hampered by

bad flight conditions. Fog is common during warm advection periods, and convection with icing is equally recurrent during periods of cold advection. Therefore, flight observations are mostly done over the open water along the MIZ, or over the mostly solid ice deeper in the Arctic.

This thesis describes a scientific mission deployed to measure the fluxes of momentum and sensible and latent heat (SH and LH) across the MIZ in the Greenland Strait. Figure 1 illustrates the broad area under investigation and depicts where warm water in the Irminger Current (IC), cold water in the East Greenland Current (EGC), and the MIZ interact. The boundary between the two currents creates an ocean front in the strait with a temperature gradient of approximately 1°C/km. This may generate baroclinic instability in the lower atmosphere above which, especially in winter, frequently gives rise to frontogenesis and development of PLs in the area (Chechin et al. 2017). These developments can be notoriously fast, and present considerable challenge to forecasters as well as sea traffic.

The data-gathering mission consisted of 7 flights on 6 days between 24 April and 9 May 2017, flown by the Naval Postgraduate School (NPS) Twin Otter. Late spring is when ice cover in the Greenland Strait is historically at its maximum. Flights began and ended at Ísafjörður Airport, Iceland. Storms and fog were avoided as much as possible, which resulted in many days where flights did not occur.

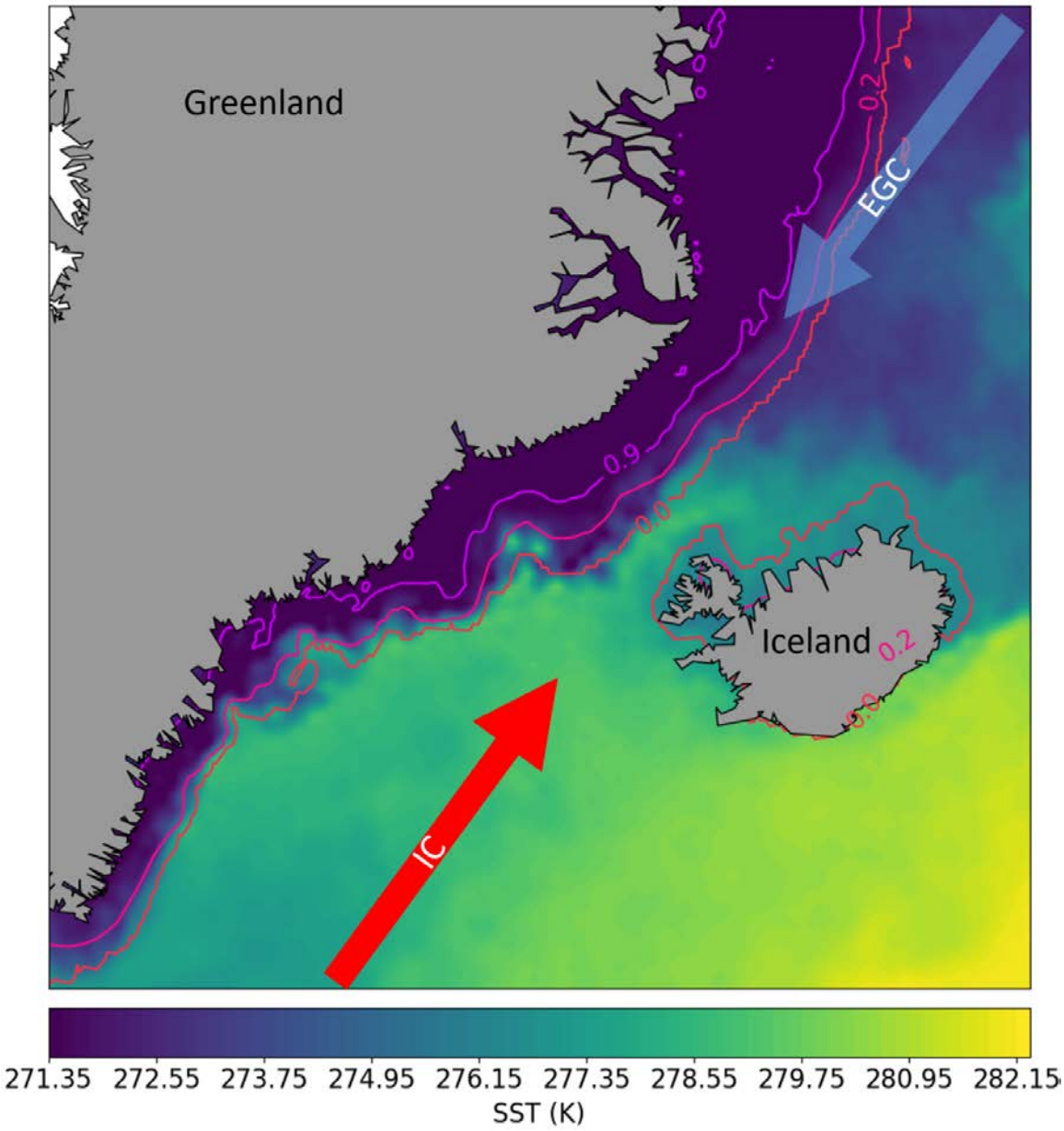

General area and direction, of Irminger Current (IC) is indicated by the red arrow and East Greenland Current (EGC) by the blue arrow. AVHRR derived ice concentrations of 90%, 20%, and 0% are indicated with contour lines.

Figure 1. AVHRR derived sea surface temperature for April 24, 2017

Three goals of this thesis are to 1) compute ice concentrations from photographs taken by a camera mounted in the belly of the aircraft, 2) explore possible correlations between coefficients such as the neutral drag coefficient (C_{DN}) and ice concentration or wind speed and 3) determine surface fluxes of latent and sensible heat in the vicinity of

and within the MIZ. The organization of this thesis is as follows. Chapter II describes the dataset and the first quality control (QC) process of filtering the data. Chapter III is the introduction of theories including covariance and bulk flux theory calculations. Chapter IV details the methods and is broken into three parts; QC, bulk flux calculations, and defining ice concentrations. This includes a brief discussion of machine learning (ML) techniques, which were used to analyze photographs from the Nadir camera. While machine learning and deep convolutional neural networks (DCNN) were used, they are not the focus of this thesis. An in depth discussion of the methods can be found in the Appendix. Chapter V is a discussion of results. Chapter VI presents the final conclusions, as well as future work possibilities which mostly involves the need for more data.

II. DATASET

Seven flights were flown from Ísafjörður Airport, Iceland. The flights were named by the recording equipment as flight numbers (FN); FN = 589 on 24 April 2017, FN = 591 on 26 April, FN = 592 afternoon 26 April, FN = 605 on 3 May, FN = 611 on 4 May, FN = 614 on 9 May, and FN = 617 on 11 May. Figure 2 shows all seven flights overlaid on satellite derived ice concentrations from 4 May, which is not indicative of ice conditions for all flights but gives some indication of the MIZ location in relation to the flight path. Table 1 lists the sensors onboard the Navy Twin Otter.

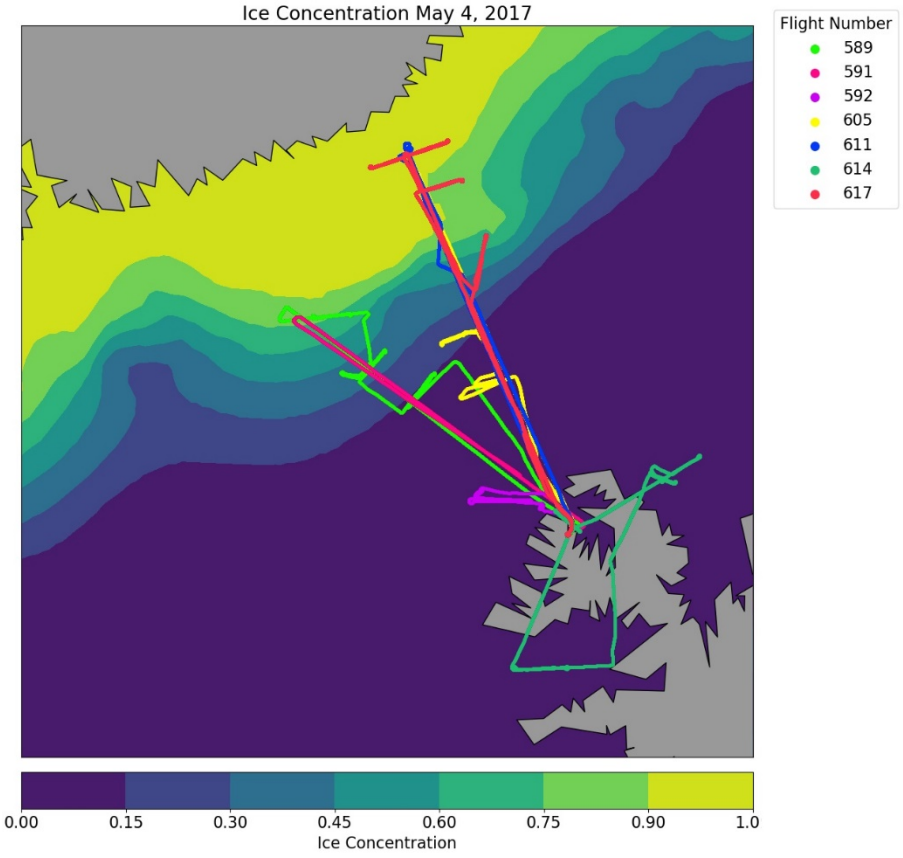

Figure 2. All flight paths studied overlaid on AVHRR ice concentrations on 4 May 2017

Table 1. Instruments onboard Navy Twin Otter

Measurement	Instrument Make/Model
Ambient Temperature	Rosemount E102AL
Dew Point	Edgetech 137-C3
Fast Humidity	Licor-7500
Flow angle Radome	Radome (4 Setra 239)
SST	Heitronics KT19.85II
Nikon Camera	Nikon D750
GPS, Platform position, velocity, attitude (pitch, roll, heading), time	C-Migets-II/Systron Donner
GPS (Back-up)	NovAtel GPS
Radar Altimeter	Collins ALT-50
Platform heading, attitude, pitch, roll (Back-up)	Trimble

A. DATA COLLECTION

Raw sensor data was recorded at 100 Hz. Flow angle measurements from the radome were combined with GPS and platform attitude measurements from the C-MIGITS_III to calculate 3-D winds. The Edgetech Dew Point sensor is too slow for use in flux calculations, so a fast responding Licor-7500 water vapor density sensor was used for latent heat flux calculations. The nadir looking Nikon camera imaged the surface under the aircraft at 1 Hz for characterization of the ice concentration.

B. QUALITY CONTROL

As with any data-set of this type, a rigorous QC process must be employed to remove irregularities and biases from the data. One example of a commonly recurring irregularity was a large spike in wind speed that occurred when the heading changed from -179.9 to 179.9 as the algorithm thought the wind direction had shifted 359 degrees. While this was easily attributed and fixed, other issues must be addressed to ensure scientifically sound methods were used.

C. DATA SUBSETTING

For each flight, data was isolated into contiguous periods of time when the aircraft flew straight and level; each of these periods are referred to as a "leg," each of which was split into multiple sub-legs later. Straight legs were required because when the aircraft turned the IR sensor was not pointing directly below the aircraft which may have led to an incorrect sea surface temperature (SST) reading. Level legs were necessary for two reasons, 1) reducing variables such as wind speed, and temperature to ten meters and ultimately the surface (discussed in Chapter II) requires a reference height which remains as constant as possible, and 2) because when the aircraft climbed or descended rapidly, the sensors would sometimes yield false readings. Figure 3 shows a spatial plot of one flight with straight legs highlighted by colors other than royal blue, Figure 4 shows the same legs highlighted with corresponding colors on an altitude plot. Straight legs were classified as those during which the aircraft did not deviate by more than one degree in heading, while legs were considered to be fl0at if altitude deviated by less than 15 meters.

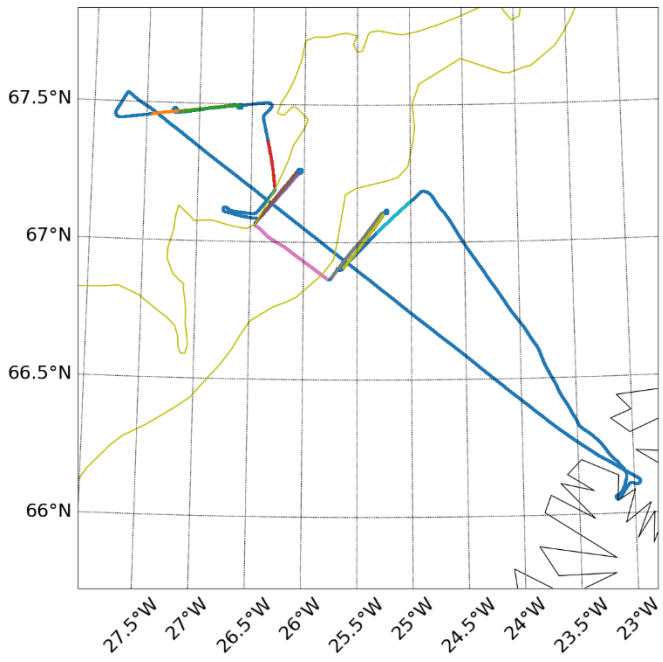

Yellow is the MIZ, black is Iceland.

Figure 3. Flight 589 track with straight legs highlighted in colors other than black

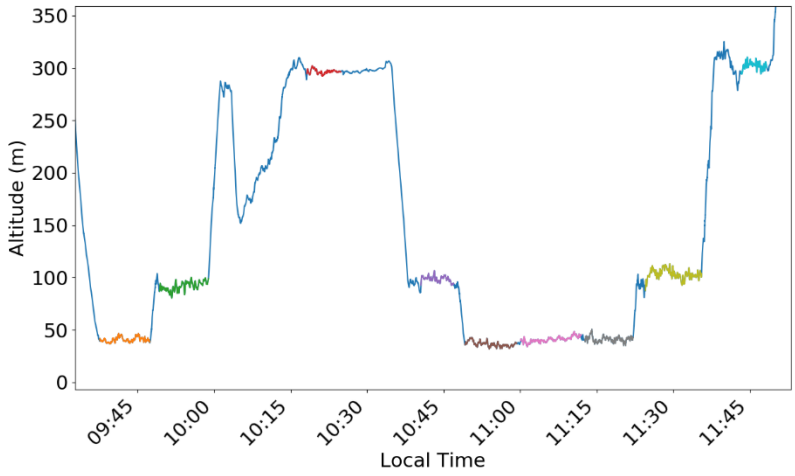

Figure 4. Portion of Flight 589 altimeter with level legs highlighted

Surface fluxes must be calculated from variables measured within the boundary layer if the aircraft measurements are to be coupled to the surface layer. In the Arctic, the

atmospheric boundary layer (ABL) is typically much shallower than at mid-latitudes with depths typically less than 150 m (Tjernström 2005). The coupling also requires conditions near neutral stability (Chapter III). Data analyzed was further reduced by using these two criteria. Specifically, only data from legs with a mean altitude at or below 100 m were considered. This significantly reduced the magnitude of data processed and improved total computational time. Stability could be determined over open water by comparison of SST and the ambient temperature measured by the aircraft. Over fractional ice the SST was unsuitable for this and the COARE iteration method was used instead.

1. Resampling

Data were recorded at 100 Hz; data for filtered legs were complete with 100 recordings every second. However, not every data point was recorded 0.01 s after the previous one. In order to ensure statistical calculations worked correctly each leg was resampled at 100Hz with 0.01 s intervals. This was accomplished using a fast Fourier transform to resample at a regular interval using a Hamming window in the python library scipy (Oliphant 2007). This was done before subdividing the legs into sub-legs in order to alter the data as little as possible.

2. Band-Pass Filter

A slight “whistle” was found in one tube of the Radome and had to be corrected. Figure 5 is a picture of the front of the NPS Twin Otter where the Radome tube intakes are located. When a large volume is connected to a thin tube, a resonator system is created. The fluid within the thin tube cannot be compressed as much as the fluid within the larger volume. The fluid within the tube will move while the volume compresses (Kinsler et al. 2000). Blowing over the rim of an empty bottle to produce a low whistle is a relatable example. As air is blown into the bottle, the air in the neck of the bottle does not compress as much as the bigger volume of air in the main part of the bottle. Air in the neck will move back and forth causing a vibration, as the air in the bottle acts as a spring. Wind direction and speed time series contained obvious spikes that usually centered on 17.1 Hz and 9.55 Hz. Other studies using data from the same sensors may not have been affected by this after down-sampling to 10 Hz. However, at 100 Hz the whistle was easily apparent and

required correction. A band-pass filter was employed to eliminate the whistle before subdividing the legs, again in order to alter the data as little as possible. Before filtering the data, the data was detrended and the mean value over the duration of the leg was removed. Any trend was added back to the band-pass filtered signal to retrieve the original data with the whistle removed. Figure 6 shows a sample of vertical wind speed at 100 Hz from the same leg as Figure 7 before and after applying the filter. The blue (orange) lines indicate the time series before (after) the whistle was removed. In the unfiltered time series, spikes in wind speed are clearly separated by 0.06 s.

Figure 5. Nose of NPS Twin Otter where Radome tube intakes are evident (black circles)

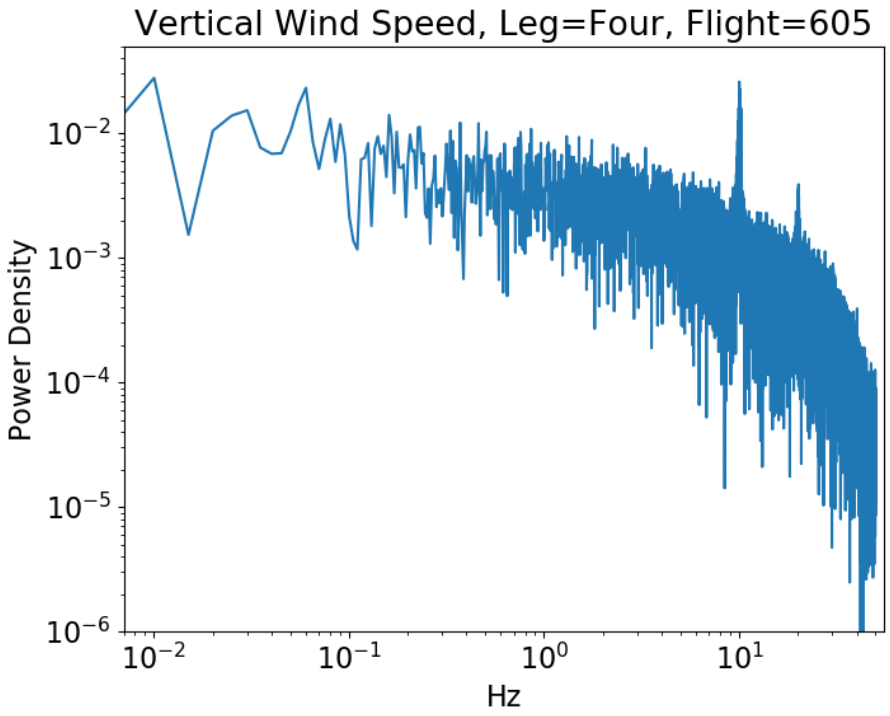

Figure 6. Example power Spectrum of vertical wind speed. Spikes at 17.1 Hz and 9.55 Hz are apparent

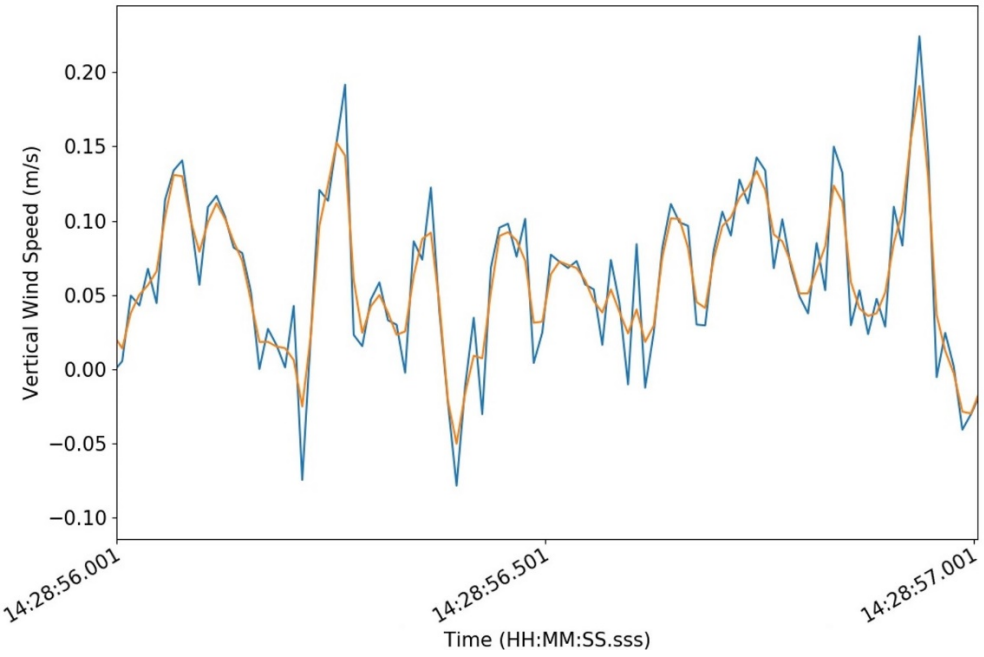

Figure 7. One second time series of *w* before (blue) and after (orange) band-pass filter is applied

3. Subdivision of Legs

Legs were split into 60 second duration sub-legs, resulting in 132 sub-legs (referred to as legs hereafter) having no overlap and 6000 data points per leg. The average length of each leg was 2.93 km. This is considered a good balance between sampling the energy of the turbulence and avoiding spatial non-homogeneity effects (Geernart 2002; Kalogiros and Wang 2009).

III. BULK FLUX THEORY

The unique contribution of this work is that it attempts to correlate fluxes and coefficients of drag, heat, and moisture to ice concentration over the MIZ. Fluxes at flight level are derived directly from flight level measurements using widely accepted equations (Andreas et al. 2010):

$$\tau = -\rho\overline{u'w'} \tag{1}$$

$$SH = \rho C_p \overline{w'\theta'} \tag{2}$$

$$LH = \rho L_v \overline{w'q'} \tag{3}$$

Where C_p=1004 J kg^{-1} K^{-1} is specific heat for dry air, L_v=2.5 × 10^6 J kg^{-1} K^{-1}, θ is potential temperature, q is specific humidity, τ is stress, ρ is density, w is vertical wind velocity, u is horizontal wind velocity, an overbar indicates an average for the leg, and a prime indicates a perturbation from a mean value. From equation 1 the frictional velocity can also be obtained;

$$u_*^{\,2} = \frac{\tau}{\rho} \tag{4}$$

Within the ABL, when neutral stability occurs $\left(\frac{\partial\theta}{\partial z} = 0\right)$, fluxes are expected to remain constant, therefore wind speed, and q will decrease logarithmically with height from the top of the ABL to the surface. When no direct measurements of surface fluxes are available, and neutral stability cannot be established empirically, bulk-aerodynamic formulas must be used to create the profile and find fluxes at desired levels. In the 1940s Monin and Obukhov proposed that a profile of near-surface momentum, sensible heat, and latent heat fluxes would follow a modified logarithmic profile within the ABL, which is now known as Monin-Obukhov similarity theory (MOST; Monin et al. 1954; Obukhov 1971). MOST has been widely used in boundary layer studies since. Their method identifies near stabile conditions and incorporates it into the profile. Methods of finding

the empirical functions of this modified profile are varied because parameters such as friction will vary with the surface roughness of each study (Vickers et al. 2013). As no known method exists for finding this profile above varied ice conditions, multiple methods were used and compared in this study and will be discussed in Chapter IV.

The Monin-Obukhov empirical functions are used to obtain a coefficient that can then be used to determine the surface fluxes using bulk formulations (Petersen et al. 2008):

$$\tau = \bar{\rho} C_{DN} (U_{10N} - U_s)^2 \tag{5}$$

$$SH = \bar{\rho} c_p C_{HN} (U_{10N} - U_S)(\theta_S - \theta_{10N}) \tag{6}$$

$$LH = \bar{\rho} L_V C_{EN} (U_{10N} - U_S)(q_S - q_{10N}) \tag{7}$$

The widely accepted equations for the coefficients C_{DN}, C_{HN}, and C_{EN} are those formalized by Garratt (1992):

$$C_{Dz} = \frac{k^2}{\ln\left(\frac{z}{z_0}\right) - \psi_m \left(\frac{z}{L}\right)^2} \tag{8}$$

where k is von Karman's constant = 0.4, z = height of measurement, z_0 is the roughness length, L is the Monin-Obukhov "length" for finding stability, and ψ_m is an empirical stability function. Many methods for finding z_0 and L exist that depend on environmental factors such as surface roughness. As there are no known methods specifically designed for the MIZ, four methods were used to investigate the data and see which fit would best describe this environment, and these are described in Chapter IV.

Three methods for calculating bulk flux are described in this study with a focus on the COARE method. All methods are found in the Air-Sea MATLAB toolbox (Sea-mat/air-sea 2019) developed for COARE (Fairall et al. 2003). The Large and Pond method (Large and Pond 1981) was used over open ocean in moderate to strong winds. The Smith method (Smith 1988) was used for fluxes as a function of windspeed and temperature also over open ocean. The Vera method (an unpublished manuscript by E. Vera 1983 described in Large et al. 1994) attempted to fit a curve to all of the published data where:

$$u_*^2 = 10^{-3}(2.717U_{10} + 0.142U_{10}^2 + 0.0764U_{10}^3) \quad (9)$$

COARE is a method that iteratively finds Z_0/L through a series of guesses that ultimately converge on a solution if the environment is neutrally stable as outlined in Fairall et al. (2003). When the iteration is run, two things can happen, either solutions start to converge or some will converge while others move steadily away from a solution. Either case stops the iteration and if convergence does not occur, the leg is not used because stability cannot be established.

The Charnock constant is used in the Large and Pond (1981) and Smith (1988) methods. Charnock (1958) proposed a constant to be used when finding z_0:

$$z_0 = \alpha\left(\frac{u_*^2}{g}\right) \quad (10)$$

where $\alpha = 0.012$ is the Charnock constant, and $g = 9.81$ m s^{-2}. Since Charnock's assertion, the value of the constant α has been studied in models, datasets, and experimental wave tanks, and typically ranges between 0.011 and 0.018 depending on environmental factors such as wave age, wave steepness, and fetch limitations (Smith 1998). In order to investigate the frictional and wave dampening effect of ice coverage, all calculations were done in two separate ways. One was with a constant $\alpha = 0.011$, the other allowed the Charnock to increase with increasing ice concentration:

$$\alpha = 0.011 + (0.007 * ice) \quad (11)$$

where ice is a ratio of $\frac{area\ of\ ice}{total\ area}$ directly under the aircraft during the flight leg. Determination of ice concentration is explained in Chapter IV and the Appendix. It was determined that the surface wind speed had much greater impact on C_{DN}, and therefore the fluxes, than ice concentration did, and this will be discussed more in Chapter V.

THIS PAGE INTENTIONALLY LEFT BLANK

IV. METHODS

Establishing surface fluxes within the MIZ is the primary goal of this thesis. In order to get to the fluxes bulk fluxes must be calculated, the resulting calculations must be checked for quality and consistency, and the ice concentration must be established for each sub-leg. The following sections explain how each of these was done.

A. BULK FLUX CALCULATIONS

Bulk flux calculations are obtained using the MATLAB air-sea toolbox converted to python. Inputs were the time series of atmospheric measurements at aircraft altitude, and outputs are the variables reduced to 10 m above the surface. Equations 6 and 7 were used to calculate the surface fluxes from the output.

B. DATA PROCESSING

Before data analysis, additional checks were completed to ensure that the stability requirements had been met, the turbulence was within the sub-inertial wave spectrum, and instruments performed properly.

An initial cross correlation of $u'w'$, $w'\theta'$, and $w'q'$ was performed so that each leg could be checked for quality and ensure that the turbulence was within the sub-inertial range. The Kalmogorov slope is a theoretical slope proposed by the mathematician Andreĭ Kalmogorov (1970), which states that the power spectrum in wavenumber space of turbulence above the sub-inertial range decays at a 5/3 rate on a logarithmic scale. In other words, if it does not, then mesoscale dynamics may play a strong role in the power spectrum, and adjustment of data at aircraft altitude to 10 m above the surface would not be possible. Figure 8 provides examples of a leg in which the power spectrum decayed at 5/3 (Figure 8a) and two legs in which it did not (Figures 8c, 8e,). In the left column of Figure 8, two example power spectra (in wavenumber) are shown including a red line at -5/3 slope for comparison. Figure 8b is an example where the spectrum does not follow the -5/3 slope because there is too much power in the high wave numbers. Legs with such characteristics are indicative of mesoscale dynamics and were excluded from the study.

Another way of illustrating this is by means of ogives. The ogive indicates where the power resides within the sub-inertial wave spectrum and that no larger or smaller-scale power is evident. An ogive of a leg that only has power in the sub-inertial range will look like an “S.” In other words, the power will be minimal at lower wave numbers, increase rapidly within the sub-range, and then have no power added in the higher wave numbers. Figures, 8b, 8d, and 8f show, respectively, an ogive for a leg in which the power spectrum followed a -5/3 slope and ogives for two legs in which it did not. The ogive depicted in Figure 8f starts out with excessive power at very low wave numbers. Ogives that do not follow the “S” pattern are also indicative of mesoscale dynamics and the leg was excluded.

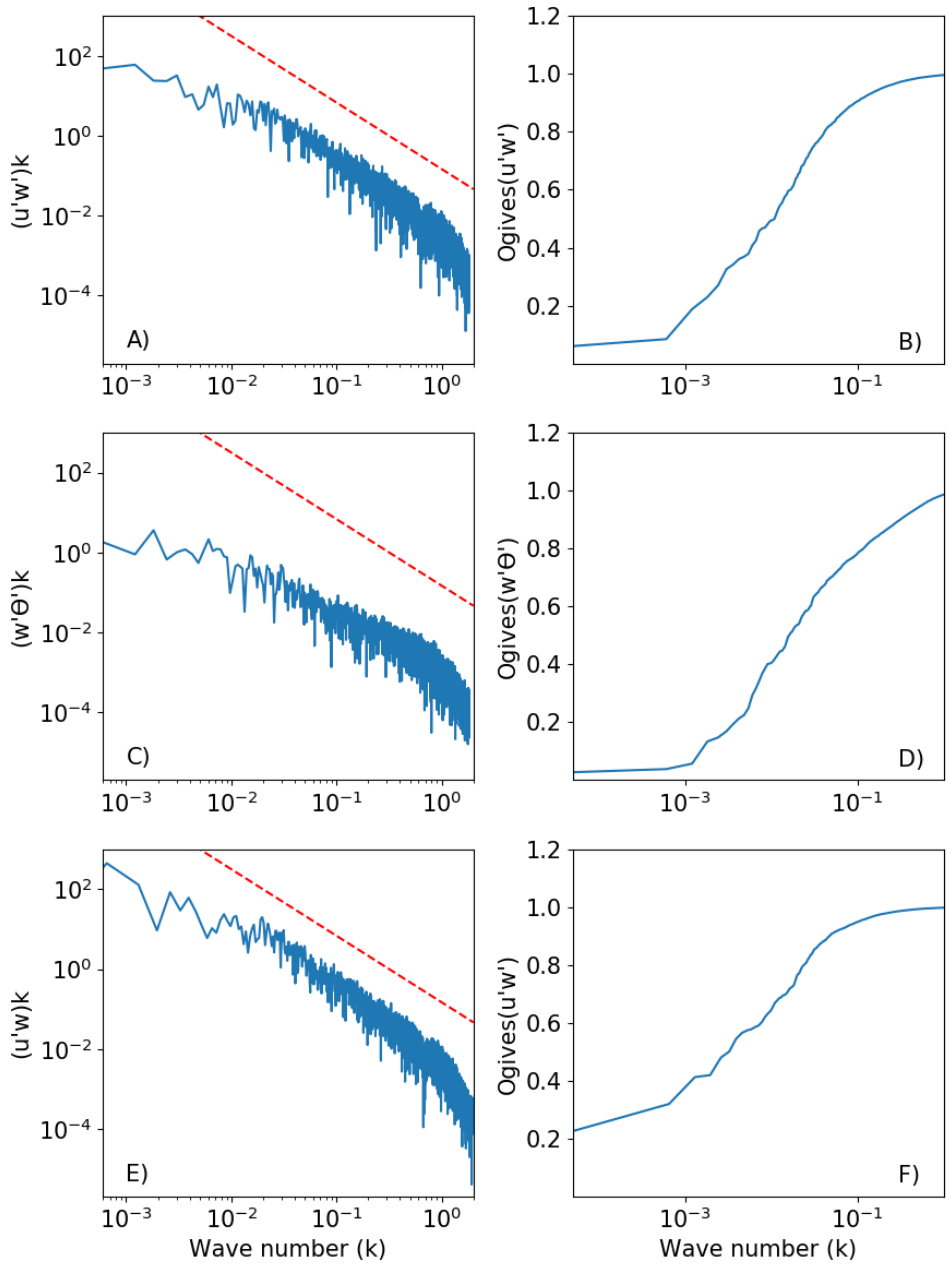

Corresponding ogives are displayed in the right column.

Figure 8. Examples of power spectra (blue) depicted in the left column with example lines plotted at a -5/3 slope (red)

C. CALCULATION OF ICE CONCENTRATION

Determination of ice concentration beneath the airplane at any given time turned out to be non-trivial. Although data assimilation for models is a constantly evolving field,

it proved unsatisfactory for our purpose. The Global Forecast System (GFS) model assimilates ice data as it becomes available; however, this happens no more than once per day; the previous day's data is used until new data becomes available (NCEP 2019). While measures are taken during data assimilation to keep the model from being overly distorted by missing data, the MIZ is a very dynamic area. Ice areal coverage during this study changed O($10km^2$) during hour long flights. Models must use some parameterization to describe the effects of ice coverage and ice concentration on the total heat budget between atmosphere and ocean. This study seeks to improve the understanding of these parameters.

A six step process was used to determine scientific usability of the data. Of note is a rigorous QC process, and the use of machine learning to determine the ice concentration along the flight path from the photographs taken from the aircraft. Manual comparisons of ice concentration data from satellite sensors and assimilation models with photographic observations showed the former to be inadequate and unreliable. It was therefore decided to use the photographs for determination of ice concentration. Manual analysis of tens of thousands of photographs, however, is inefficient; therefore, the use of artificial intelligence and ML techniques were employed for this purpose.

One of the goals of this study is to determine how fluxes change with respect to ice concentration. Ice concentrations are used in both atmospheric and oceanographic models, and parameters such as LH and SH are derived from that during assimilation. Accurate representation of ice concentration is limited by the grid spacing of the model and by the resolution of the instrument recording it. Different models require ice concentrations for various reasons. An atmospheric model would use it to define boundary conditions of surface heat fluxes over time and surface friction. The MIZ is a very dynamic region where the location of constant concentration contours moved tens of kilometers during a four-hour flight. Extracting ice concentration from surface temperature readings proved unfruitful. An algorithm that seemed to extract ice concentration from surface temperature readings on one leg would not work well on another leg. As an example; one such trial algorithm used freezing point because most temperature readings of water within the MIZ are close to freezing point and lower readings could be assumed to be ice. However, freezing point changes with salinity and salinity changes with age of sea ice because salt

slowly drains out of sea ice. Figure 9 is an example of a photo of the ice and water surface to illustrate the different surface conditions that were encountered within close proximity. These measurements taken from aircraft flying level and straight measuring SST at 100Hz gives widely varied data. Figure 10 suggests that correlations between estimated SST and ice concentration are visually obvious; for example, lower SSTs were detected when more ice was present, and more SSTs at the freezing point were detected when more water was present. However, obtaining accurate signals of ice concentration with this method was not successful. The process was not totally useless as it gave a data point for quality control of the next iteration which was to get ice concentration from pictures, and legs where all SST readings were above -1°C or below -2°C could be respectively considered 100% water ice ice.

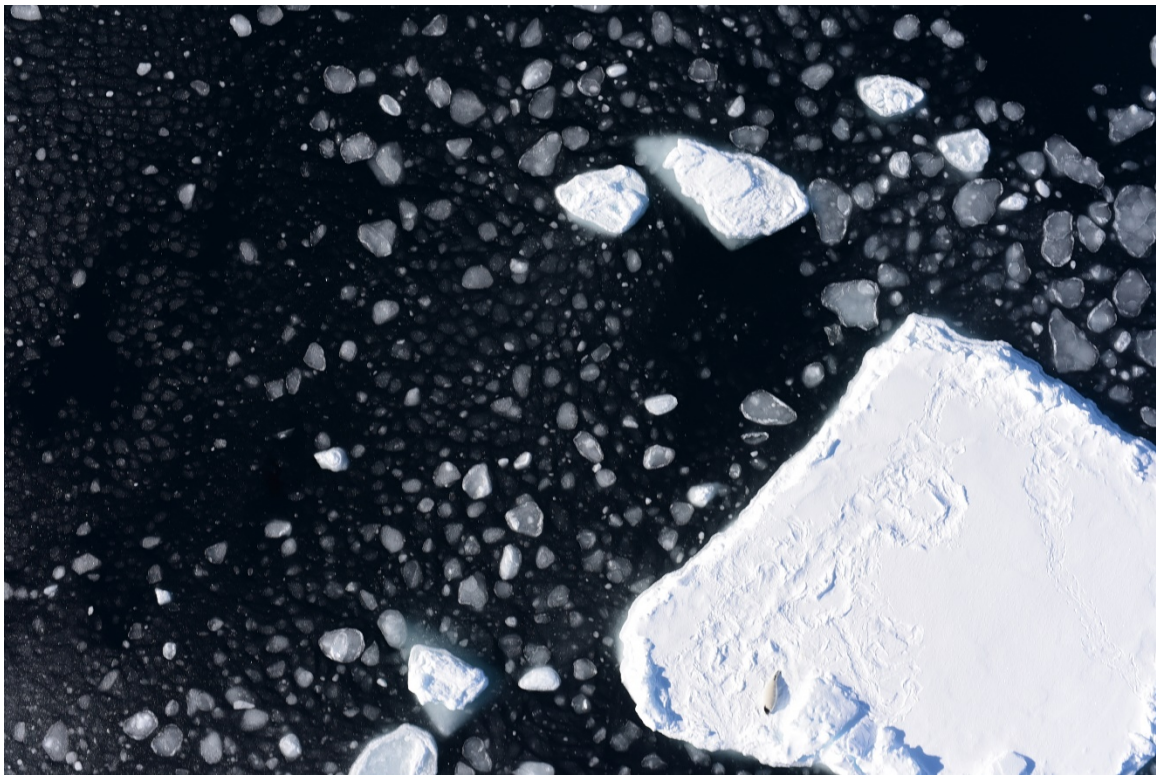

Figure 9. Picture taken from downward looking NIKON camera

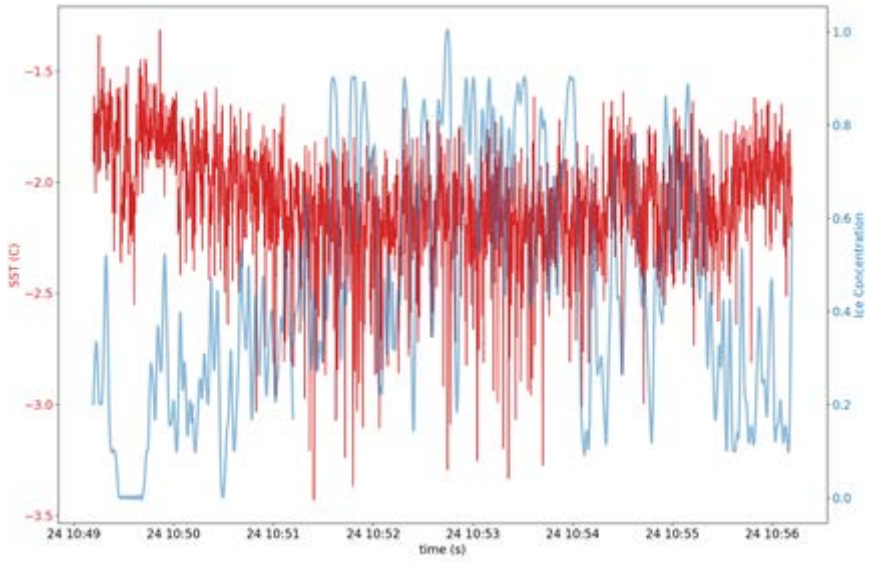

Figure 10. Time series of SST estimates derived from downward looking IR sensor (red) and final time series of ice concentration (blue)

An algorithm that analyzed the photographs and was verified visually was first employed. Each photograph was imported as a 3-axis array of red, green, and blue values 0–255 and averaged across each axis. The blue axis was eliminated due to variability (e. g sun angle caused wide distribution of blue across multiple legs), and the green and red axes were averaged separately and any value above average was set to 1 while all other values were set to 0. Ones in either array were considered ice and zeroes were considered water. Figure 11 shows an example of the filters and the resulting ice mask. When sun glint, or shadows were present, pixels were mislabeled using this method. Mislabeling made this method inadequate, so ML was used to refine the ice concentration further.

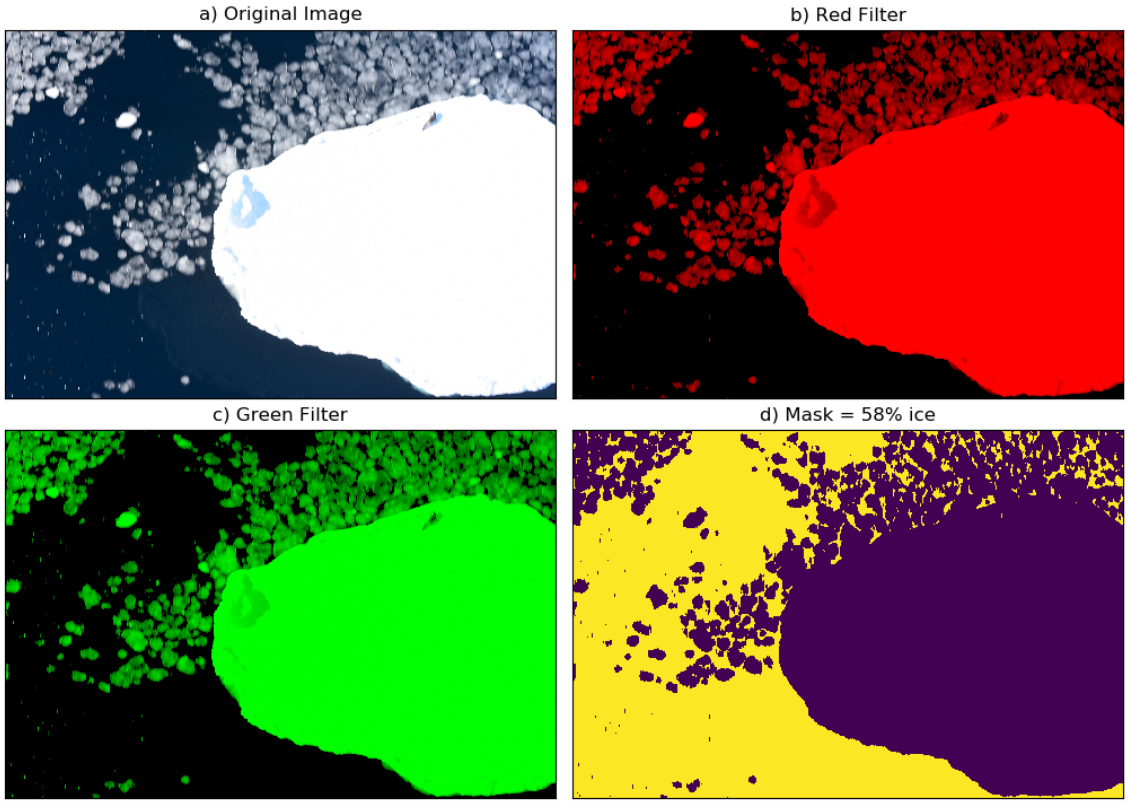

Figure 11. Example image (a), with red (b) and green (c) filters applied to obtain a mask (d) where purple is ice and yellow is water

An ML model was trained with 46 ground truth (GT) (human-analyzed) images and 15 GT validation images. Training with as many images as possible is generally better; however, creation of the training dataset is time-intensive, and the 61-image training dataset appeared to be sufficient for the purposes of quantifying ice concentration. Pixel by pixel accuracy of the model output to the validation images was consistently above 0.987 after 1000 epochs ("epoch" is a ML term defined as a time when every image has gone through the model for training). The accuracy is determined by the number of pixels correctly labeled by the model divided by the total number of pixels in the image. After training, the model assesses images and outputs a gridded array of predictions where numbers correspond to predictions. A dense conditional random field (CRF; see Appendix) was used to improve the accuracy further. The array of predictions, in this case only ones (ice) and zeroes (water), was summed and divided by the number of pixels in the image to

produce an ice concentration. This method worked extremely well, (except for areas where there was either no ice or 100% ice concentration). Areas where it did not work were inconsequential to this study as the ice concentration was already determined in those areas based on the consistently observed high or low SST. Figure 12 is an example of a) a scene with less than 100% ice concentration with b) classifications determined by the model before applying CRF for each 96x96 pixel subsection of the image and c) new classifications determined by the CRF. Any model prediction that differed from the IR sensor algorithm estimate or the color mask method by 10% or more was inspected visually and a new data point was entered manually. Pictures were taken at 1 Hz, ice concentration values for each picture was calculated and indexed with time stamps corresponding to the atmospheric measurements.

LH, SH and other variables and coefficients were directly measured at aircraft level (Equations 1–3), and derived or calculated using the Coupled Ocean-Atmosphere Response Experiment (COARE) model (Fairall 2003) when stability conditions were satisfied for the surface. Determining stability is difficult with SSTs in mixed ice conditions, so stability is considered near neutral when the COARE algorithm converged.

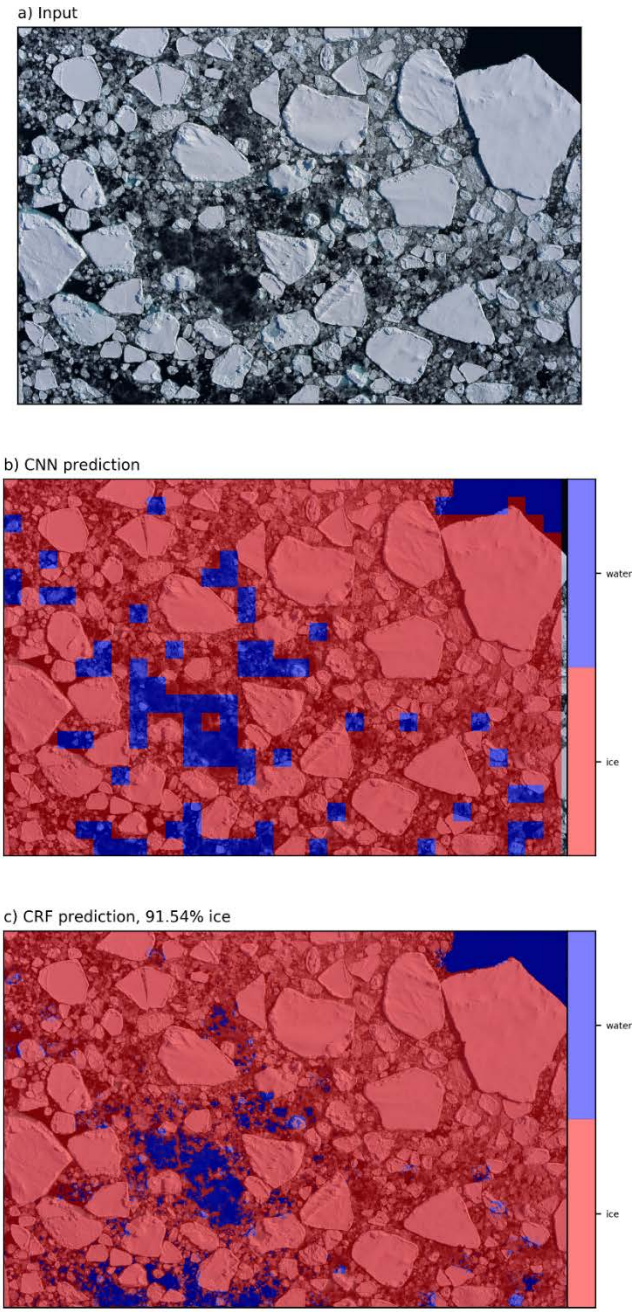

A is the original picture, b is the model designated classification of each 96×96 tile, c is the final classifications after applying CRF with determined ice percentage.

Figure 12. Classification of ice and water

THIS PAGE INTENTIONALLY LEFT BLANK

V. RESULTS

Results are presented in three sections which follow the goals of the thesis. Goal 1 was to compute ice concentrations and has been sufficiently described in Chapter IVc and the Appendix. Sections A and B correspond to Goal 2, which was to explore correlations of coefficients to ice concentration or wind speed. Use of the variable Charnock number in relation to ice concentration is followed by fluxes and coefficients in aggregate for this dataset, and comparison with accepted values in current literature. Section C explores SH and LH within the MIZ for a better understanding of the effect of surface temperature and ice.

A. VARIABLE CHARNOCK CONSTANT

The Charnock number has always been used as a constant for the environment under consideration, however the highly dynamic nature of the MIZ suggests that an adjustment may be necessary. Within COARE the Charnock constant is set to .011 with a note that this number is to be used in open ocean environments (in accordance with Fairall and Edson 2003), and 0.018 is to be used in fetch limited (coastal) areas. The MIZ covers both regimes, and in between, within a short distance. Figures 13 and 14 contain comparison plots using C_{DN} values on the y-axis and ice concentration and wind speed, respectively, on the x-axis. For comparison of datasets the reader is referred to Peterson and Renfrew (2003), and Cook and Renfrew (2013).

Figure 13 (top) shows the C_{DN} calculated using a Charnock value of .011 as a function of ice concentration. No discernable correlation to ice concentration is apparent. Figure 13 (middle) depicts use of the variable Charnock, and still no discernable effect can be identified. Figure 13 (bottom) compares the two methods on the same plot, illustrating that there is little difference between the two methods. The variable Charnock seems generally to raise the value of C_{DN}, but only by a small amount. Ice concentration shows no effect at all.

Figure 14 shows 3 plots of C_{DN} as a function of ten-meter wind speed. A clear dependence of C_{DN} on wind speed is apparent, with approximately 20% increase in

magnitude as 10 m wind speed increases from 2 to 8 m/s. Again variable Charnock raises the value of the coefficient by a small amount and causes a bit of dispersion.

In Figure 15 the values of C_{HN} and C_{EN} are shown along with C_{DN} as a function of 10 m wind speed. These values are used in calculations of surface fluxes by use of the bulk method. From Figures 14 and 15, we see little or no effect of ice concentration on the coefficients, clear dependency of C_{DN} on 10 m wind speed, C_{EN} and C_{HN} with a minimum value near a 10 m wind speed of 6 m s^{-1}, and small effect by adjusting Charnock from 0.011 to 0.018 as a function of ice concentration. The Charnock effect is ignored in the following calculations, and the value of 0.011 used throughout.

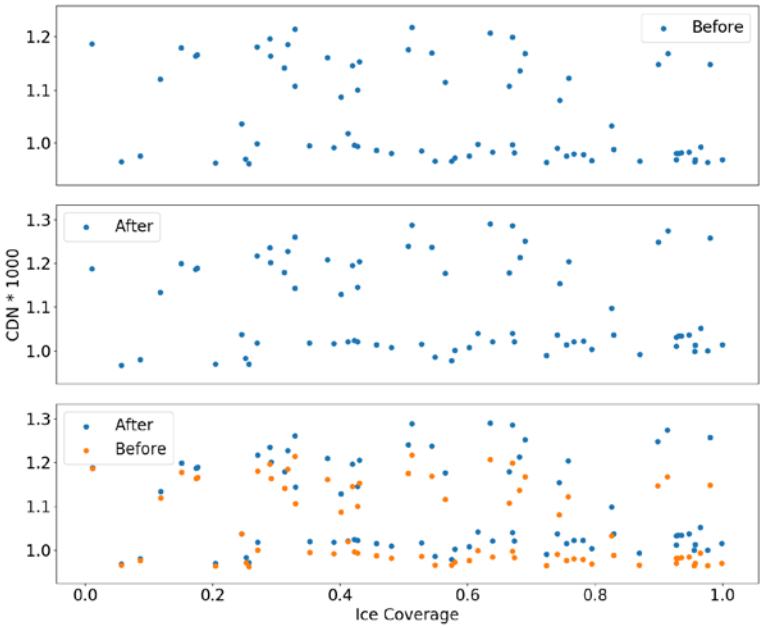

Figure 13. Comparison of data points before and after the proposed Charnock correction with respect to ice concentration

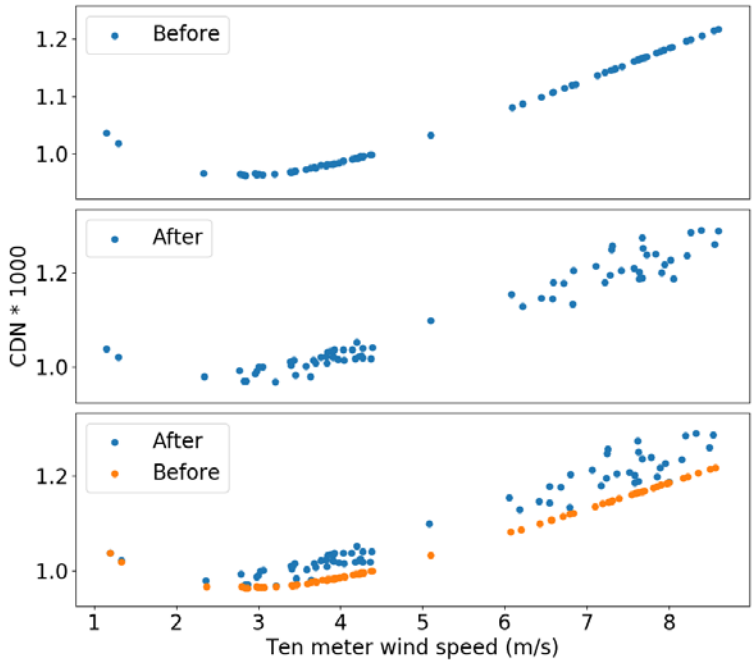

Figure 14. Comparison of datapoints before and after the proposed Charnock correction with respect to wind speed

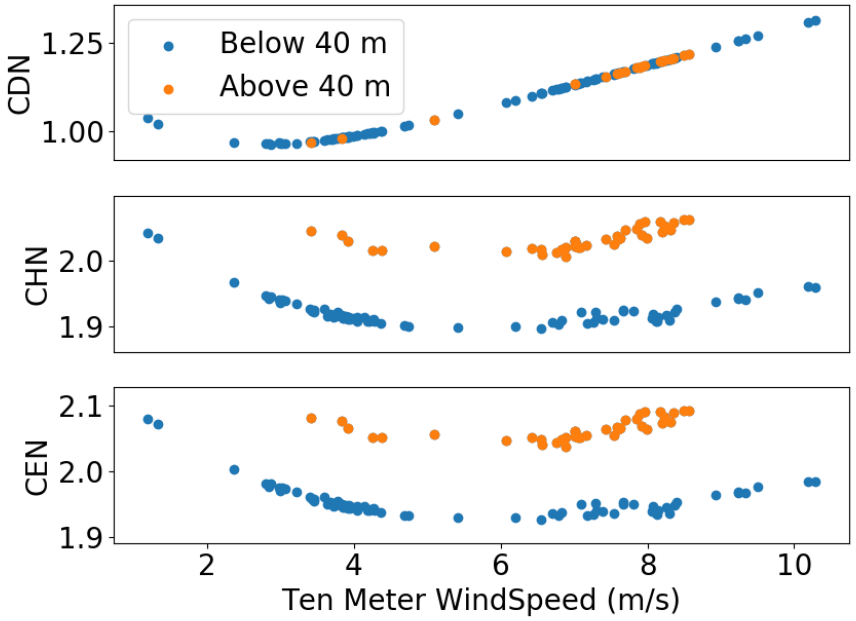

Figure 15. Coefficients of drag, heat transfer, moisture transfer vs ten-meter wind speed for all acceptable legs in the dataset

B. FLUXES VS SURFACE TEMPERATURE

Figures 16 and 17 show the results of the heat flux calculations as a function of surface temperature, calculated by eddy covariance method directly from the aircraft measurements (a panels), and by use of the COARE model (b panels). Sensible heat fluxes are shown in Figure 16, and latent heat fluxes in Figure 17. In these figures, a negative flux implies a flux from the ocean to the atmosphere.

In Figure 16, the sensible heat fluxes at aircraft altitude show hardly any relation to surface temperature, although they might have a slight negative tendency for surface temperature between -2°C and 0°C. Surface fluxes computed by COARE show some dependency on surface temperature in the -2°C and 2°C range, with flux magnitude increasing with higher SST. This range of SSTs corresponds to the transition zone between the Irminger current and the ice edge. The triple point of the ice/ocean mixture is about -1.8°C. At lower SSTs (-2°C to -5°C), the sensible heat fluxes are small, and show little dependence on SST. A couple of data clusters over the Irminger current (SST ~5°C), show on one hand near-zero SH, and fluxes of opposite sign over the East Greenland Current in the other.

Latent heat fluxes (Figure 17) show a similar lack of general relationships. At aircraft altitude the covariance figures are within 20 W m^{-2} of 0 but show no significant correlation. For surface LH computed using COARE, a subset of the data shows a correlation, with flux magnitude increasing with surface temperature in the -5°C to -2°C range. Three clusters of data show up outside the trending points, two of which are over the Irminger current, separated by a factor of two, but all negative, indicating that the underlying surface was in all cases transferring heat to the atmosphere.

These data were obtained on different flights, under different weather conditions. It seems clear from Figures 16 and 17 that environmental factors other than surface temperatures influence the heat fluxes. These factors were probably similar in the cases for subsets of data in which a correlation seems visually apparent, but dissimilar among the others.

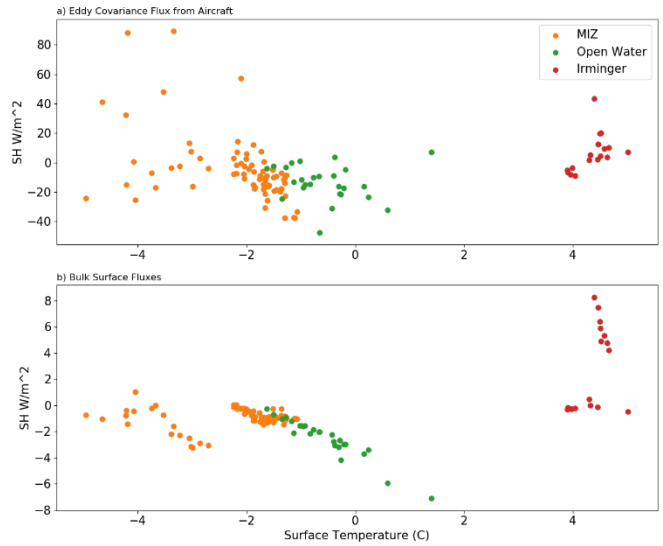

Figure 16. SH as a function of surface temperature over the MIZ, cool open water, and IC

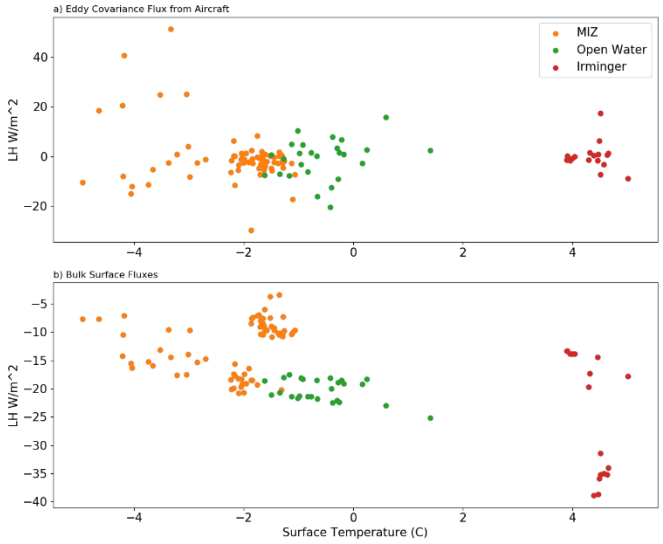

Figure 17. LH as a function of surface temperature over the MIZ, cool open water, and IC

C. SH AND LH VS ICE CONCENTRATION AND WIND

Figures 18 through 21 show the heat fluxes as a function of the underlying ice concentration. The panels are arranged similarly to those in Figures 16 and 17, and the data are shown color coded according to wind speed. Again flux values are negligible at aircraft

altitude, and show no obvious dependence on ice concentration. The bulk method calculation of surface fluxes however, shows weak negative values, also independent of ice concentration. This results from the earlier finding that C_{DN} was independent of ice concentration (Figure 13).

The significance of wind speed, however, is apparent in the figures. LH, particularly, increases significantly with wind speed (Figures 18 and 19). For SH (Figures 20 and 21), the effect of wind speed is not apparent, and the values appear to trend toward zero at higher winds, over a wide range of ice concentrations. Again, however, fluxes are generally weak. Figures 19 and 21 depict the same fluxes as Figures 18 and 20 respectively over the MIZ highlighted according to wind speed, however the sub-legs with winds below 5.5 m s^{-1} have been removed. Removing the lower wind speeds increases the correlation between fluxes and ice concentration.

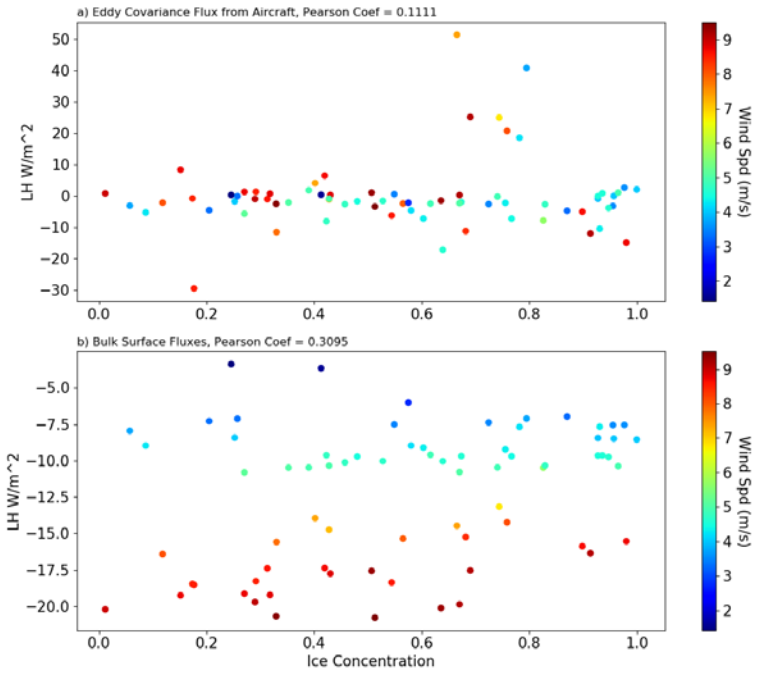

Figure 18. LH over MIZ highlighted according to ten-meter wind speed

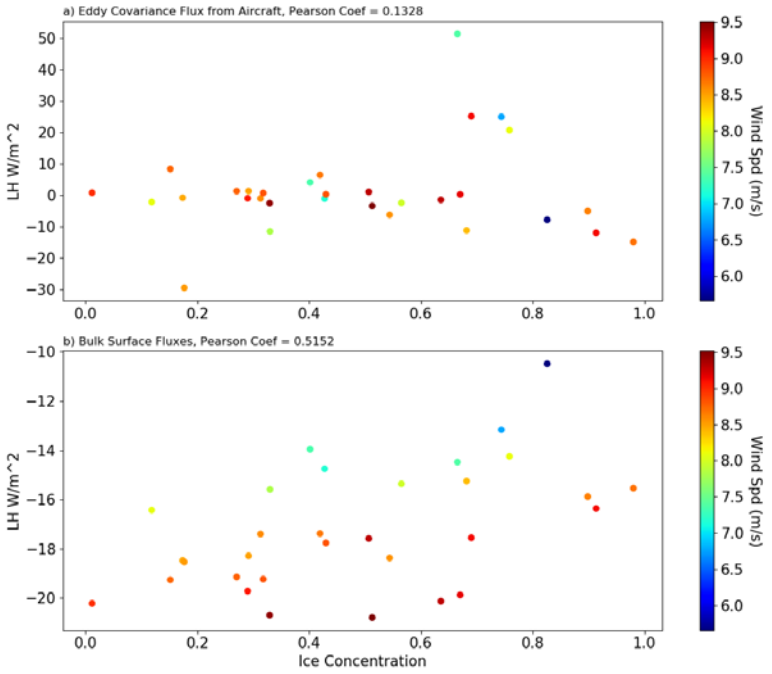

Figure 19. LH over MIZ highlighted according to ten-meter wind speed with low wind data removed

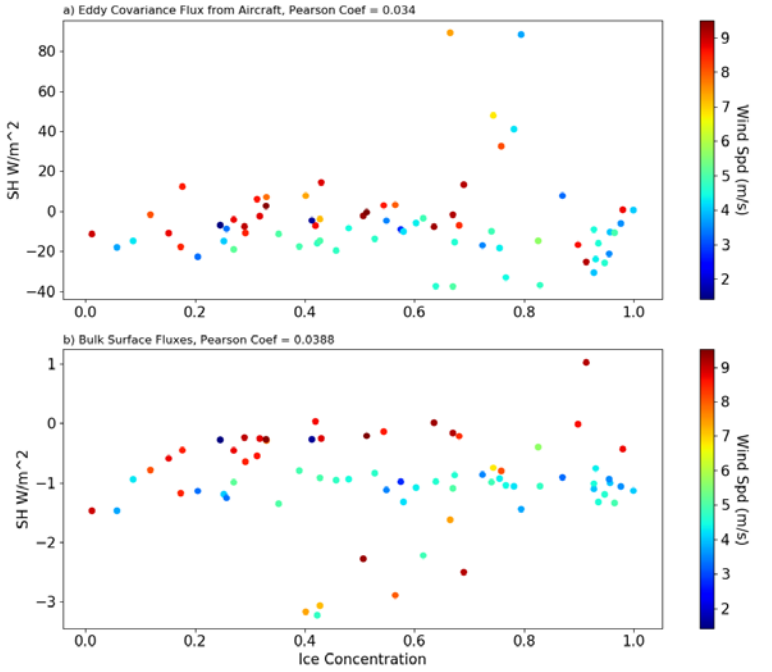

Figure 20. SH over MIZ highlighted according to ten-meter wind speed

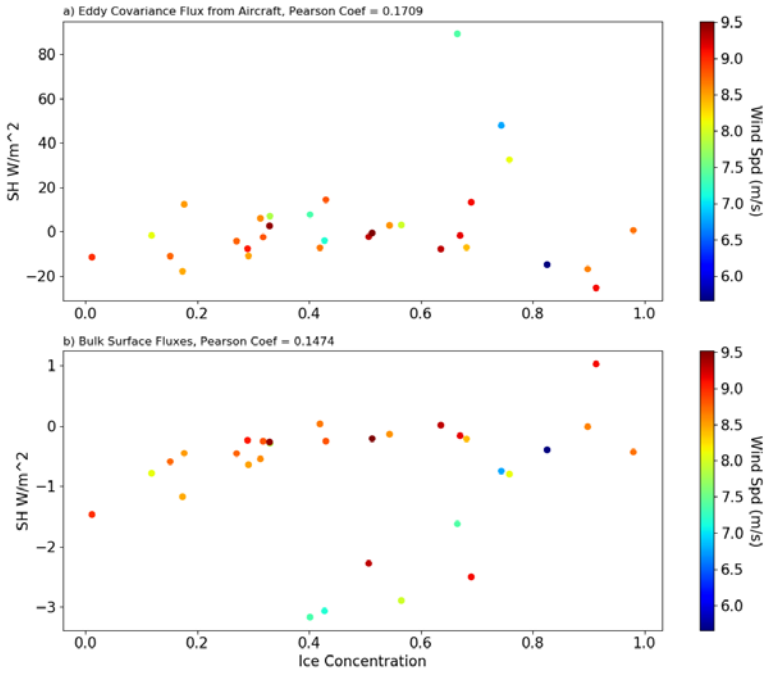

Figure 21. SH over MIZ highlighted according to ten-meter wind speed with low wind data removed

VI. CONCLUSION

Use of ML to determine ice concentration from low level photographs was critical to analysis. ML is still in its infancy and could develop to become more useful in various scientific applications. The exact method used here may not be useful for a large number of datasets because high resolution pictures of ice are not very common; however, there are many similar methods that could be employed in a broad spectrum of scientific studies. For example; using this method which subdivides pictures into "tiles" seems like it would not scale well for satellite derived images where one pixel represents 4 km^2. ML models exist that utilize masks and have training nodes that learn how to pick out regions of interest, such as the method outlined in He et al. (2018), which may prove useful. Ways to use ML in future studies where a similar calculation is needed are discussed in the Appendix and include use of other pre-trained models, other methods for extracting regions of interest, and exploring the impact of changing training variables.

No significant correlations were found between sensible or latent heat fluxes and ice concentration using eddy covariance estimates from the aircraft. However, at wind speeds exceeding above 5.5 m s^{-1}, a weak correlation was found in surface latent heat flux and ice concentration, such that the flux to the atmosphere decreased with greater ice coverage (Figure 19b). However, because the COARE algorithm is not designed to work over ice cover, the result should be considered with caution. On some flights, small heat fluxes were measured, but they did not appear to be dependent on the underlying surface temperature. Wind speed apparently was the dominant impact on heat flux magnitude. Additional data collected in a variety of environmental regimes would permit a more rigorous statistical analysis of any relationships between surface temperature or ice cover with boundary layer heat fluxes.

Flight conditions were difficult in the Greenland Strait in the spring months of 2017. Only seven flights were possible over a period of about three weeks. Fog was frequent, and icing conditions associated with frontal passages was as well. Both conditions prohibited access to the MIZ. On days that flights were possible, no foul weather was observed. Significant fluxes were also low on those days. It therefore seems that aircraft may not be a

suitable platform for flux measurements over the MIZ, and a surface platform that can withstand a variety of weather conditions, such as a ship or an ice float, may be more effective.

APPENDIX

A time series of ice concentration was needed in order to study how it correlates to air-sea fluxes. Ice concentration could not be obtained from SST readings, so a ML method was employed utilizing the pictures taken from the downward pointing camera aboard the aircraft. A full description of the data, pre-processing method, ML model and training, and post-processing method follows, and future possibilities for applying the method are discussed.

A. DATA

A total of 60,234 photos were taken from the aircraft. One photo was taken every second which gave 600 data-points for every sub-leg. Ice concentration is a ratio of ice to total area observed. AVHRR products report this in tenths where a value of 5 would mean 5/10 of a grid square is covered with ice. ML is the best method of getting this ratio for 600 photos per sub-leg. It is the best method because ice concentration could not be obtained from the SST measurements, simple computer vision techniques on the photos does not work when sun glint or shadows are present, and manual analysis of over 73,000 photos would be too labor intensive.

B. PREPROCESSING AND MASKING

Preprocessing the data for use in deep convolutional neural networks (DCNN) involved enhancing the photos, determining where ice and water is in a small sample set for training and validation, generating "masks," arrays of ones and zeros that match the photo pixels for ice and water respectively, then splitting the photos into small square "tiles." Photos were enhanced with Gaussian blur contained in the python module skimage (Stéfan van der Walt et al. 2014). The Gaussian blur enhances differences in objects and the background according to a histogram of the image. Determination of which pixels are ice and which are water is done using a python "dl_tools" module developed in Buscombe et al. (2018). This method wraps a graphical user interface (GUI) on the python module "pydensecrf" (Krähenbühl et al. 2011) which takes the pairwise potential of every pixel to every other pixel using a CRF generator and determines the likelihood that they are of the

same object. This pairwise potential can be used to give the likelihood of each pixel to be of the same classification of the human defined pixel. Figure 22 shows an example of a photo in the top frame, human identified types in the middle, and the result of the CRF on the bottom. Figure 23 is the resulting array to be used as a mask for training the model.

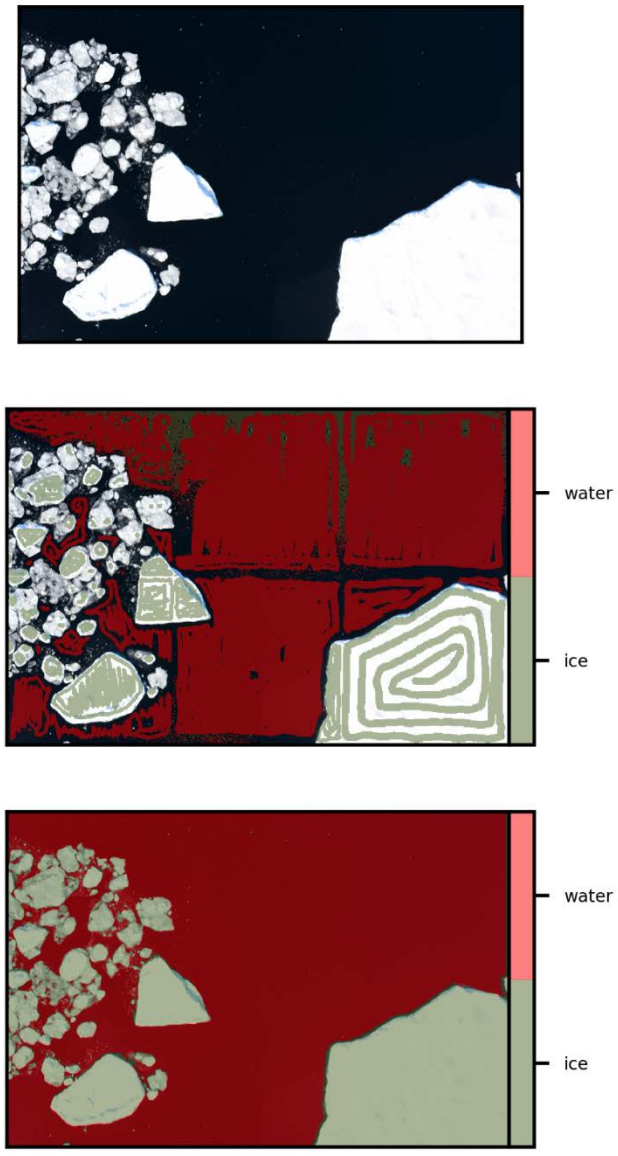

Figure 22. Example output from the “dl_tools” module for classifying images

Figure 23. Example output from dl_tools, a mask of ones and zeros for use in the ML model, ones (zeros) are depicted in black (white) and represent ice (water)

This process was completed for 61 photos on images that were 3008x2008 pixels. An algorithm was applied to each image that split the image into 96x96 pixel tiles. If a tile was 95% or more ice according to the mask, it was placed into a folder named “ice” and if it was 95% or more water it was placed into a folder named “water.” Figure 24 depicts examples of ice and water tiles. This resulted in 67,412 (72,643) tiles of ice (water), where a subset of 43,000 (45,000) were used for training and the remainder for validation. The quantity used for training and validation subsets was arbitrarily chosen. The tile size was decided as the best option for these photos from the tile sizes that the pretrained model could accept. mobileNetV4 (Sandler et al. 2019) was used in this case, and it takes tile sizes 96x96, 128x128, 160x160, 192x192, and 224x224. Sandler et al. (2019) showed similar accuracy between all tile sizes when used on the ImageNet dataset (ImageNet 2019). 96x96 is used here after looking through pictures and identifying ice chunks regularly less than 96 pixels in diameter. Theoretically the CRF would reclassify these chunks anyway, and

future work could look into the results of using different tile sizes. It is worth mentioning that other models such as Mask RCNN (Abdulla 2017) have learning nodes within the DCNN that will learn the best size and shape of tiles for the data. This method saves computing time on the inference side because it can effectively sample images rather than fully read them into memory. Future work should investigate which method is most effective for detecting ice.

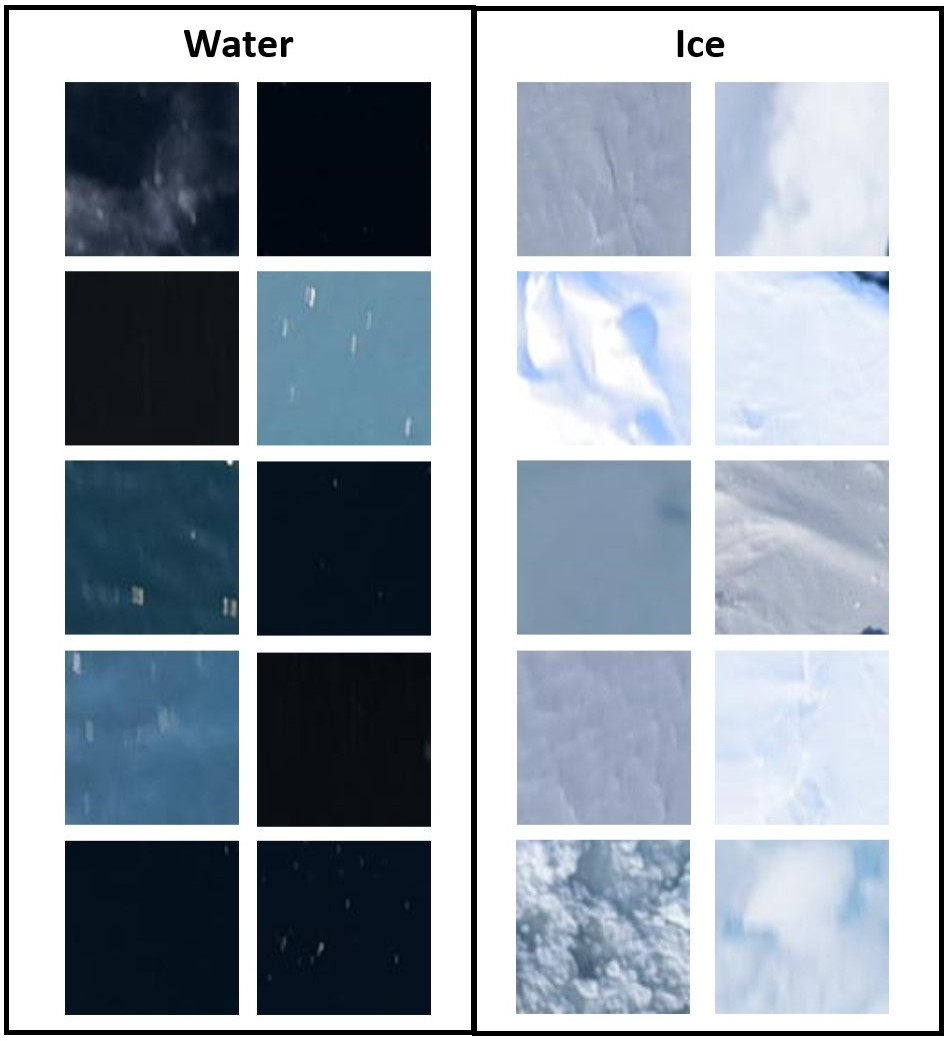

Figure 24. Example tiles of ice and water used for training

Use of a pre-trained model, one that has been trained by an organization with an array of graphical processing units (GPU) and access to millions of photos, for example

Google or Microsoft, is referred to as transfer learning (Iqbal et al. 2018). The neural network and trained "weights" for each node are shared publicly, and others can tune that model to recognize a new classification. As mentioned, mobileNetV4 was used in this case, and the process of adding learning nodes and input/output layers followed the process outlined by Buscombe et al. (2018) with minimal changes required for GPU architecture and updated python modules.

During training a tool called Tensorboard can be used to for debugging and evaluating the progression. Tensorboard is a testing and debugging tool within the tensorflow python library. Accuracy estimates are calculated periodically throughout the training by using validation images and checking the output label to the GT label, and Tensorboard is updated with accuracies and other statistics. It gave accuracy values of 98.7%, but that is a rough estimate of the actual accuracy because the validation dataset is very small compared to large size and widely varying set of images. A manual analysis of results was completed by stitching together 2,000 randomly chosen result images from the sub-legs with data being used into a video to subjectively identify obvious problems in classification. Figures 12 and 25 depict good results, which was the norm. Figure 26 depicts an edge case where reflection of bright ice onto the surface from the airplane was evaluated as ice when the water is a light color. Figure 27 depicts an example of this reflection when the ice gives good contrast, and the reflection was properly categorized.

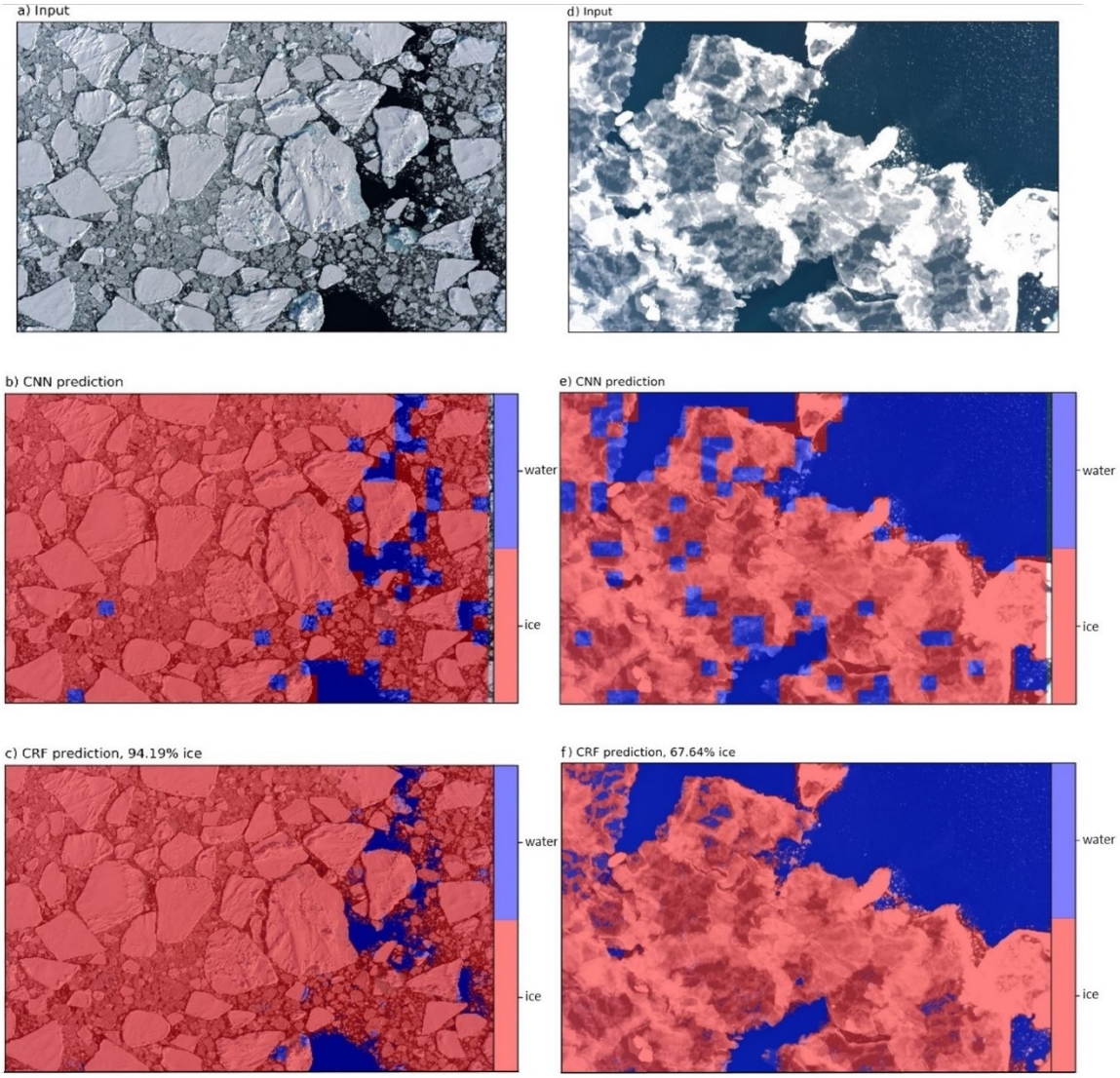

Figure 25. Good results from CNN and CRF with ice percent

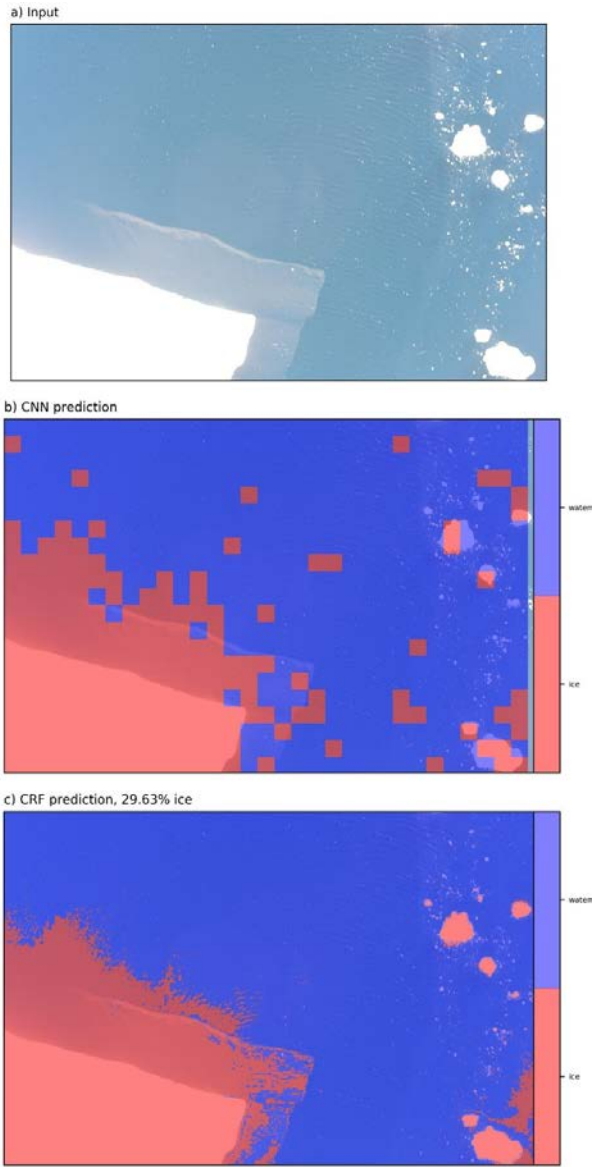

Figure 26. Results from CNN and CRF with ice percent where ice reflection led to inaccurate predictions

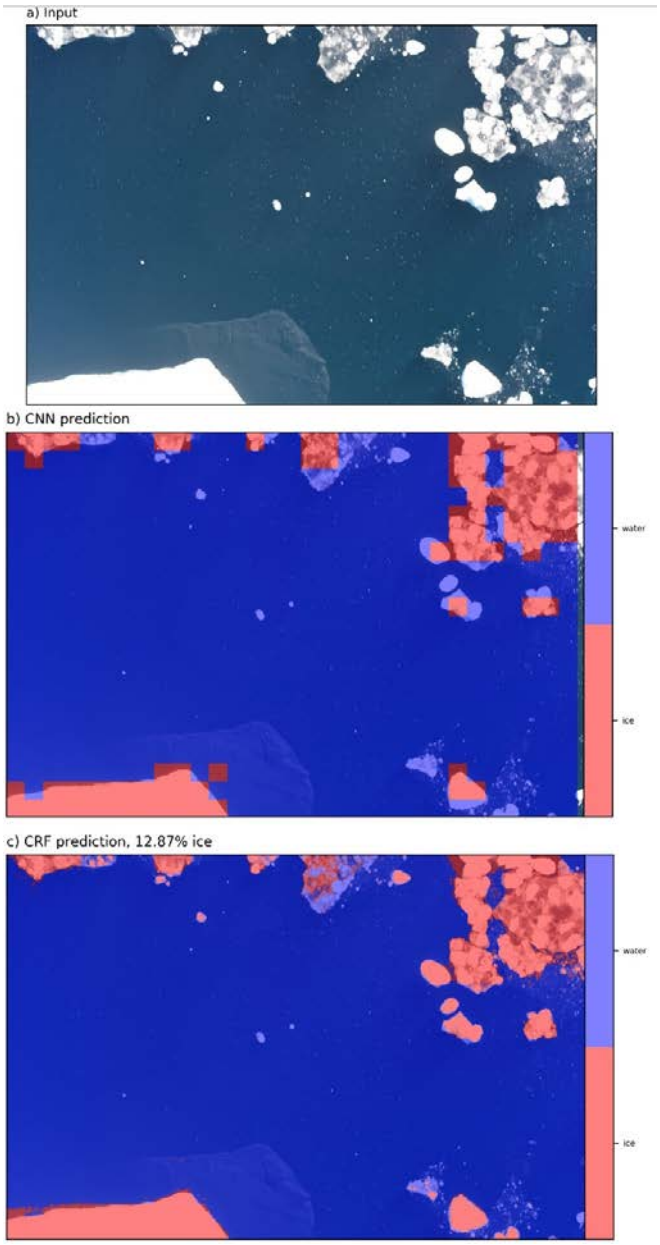

Figure 27. Results from CNN and CRF with ice percent, where ice reflection is accurately predicted

There are numerous adjustable parameters in the preprocessing, CRF, CNN, and post-processing. A future study should be done to test the effectiveness of adjusting these parameters and/or learning them. For example: using different size tiles, adjusting learning momentum, and introducing the CRF into the model so that pairwise potentials can be learned.

LIST OF REFERENCES

Adakudlu, M., and I. Barstad, 2011: Impacts of the ice-cover and sea-surface temperature on a polar low over the Nordic seas: A numerical case study. *Q.J.R. Meteorol. Soc.*, **137**, 1716–1730, https://doi.org/10.1002/qj.856.

Andreas, E. L., T. W. Horst, A. A. Grachev, P. O. G. Persson, C. W. Fairall, P. S. Guest, and R. E. Jordan, 2010: Parametrizing turbulent exchange over summer sea ice and the marginal ice zone. *Q.J.R. Meteorol. Soc.*, **136**, 927–943, https://doi.org/10.1002/qj.618.

Buscombe, D., and A. Ritchie, 2018: Landscape Classification with Deep Neural Networks. *Geosciences*, **8**, 244, https://doi.org/10.3390/geosciences8070244.

Charnock, H., 1955: Wind stress on a water surface. *Q.J Royal Met. Soc.*, **81**, 639–640, https://doi.org/10.1002/qj.49708135027.

Chechin, D. G., and C. Lüpkes, 2017: Boundary-Layer Development and Low-level Baroclinicity during High-Latitude Cold-Air Outbreaks: A Simple Model. *Boundary-Layer Meteorol*, **162**, 91–116, https://doi.org/10.1007/s10546-016-0193-2.

Cook, P. A., and I. A. Renfrew, 2015: Aircraft-based observations of air-sea turbulent fluxes around the British Isles: Observations of Air-Sea Fluxes. *Q.J.R. Meteorol. Soc.*, **141**, 139–152, https://doi.org/10.1002/qj.2345.

Fairall, C. W., E. F. Bradley, J. E. Hare, A. A. Grachev, and J. B. Edson, 2003: Bulk Parameterization of Air–Sea Fluxes: Updates and Verification for the COARE Algorithm. *J. Climate*, **16**, 571–591, https://doi.org/10.1175/1520-0442(2003)016<0571:BPOASF>2.0.CO;2.

Geernaert, G. L., 2002: On Extending The Flux-Profile Similarity Theory To Include Quasi-Homogeneous Conditions In The Marine Atmospheric Surface Layer. *Boundary-Layer Meteorology*, **105**, 433–450, https://doi.org/10.1023/A:1020307703242.

Gryanik, V. M., and C. Lüpkes, 2018: An Efficient Non-iterative Bulk Parametrization of Surface Fluxes for Stable Atmospheric Conditions Over Polar Sea-Ice. *Boundary-Layer Meteorol*, **166**, 301–325, https://doi.org/10.1007/s10546-017-0302-x.

He, K., G. Gkioxari, P. Dollár, and R. Girshick, 2018: Mask R-CNN. *arXiv:1703.06870 [cs]*.

Kolmogorov, A. N. (Andreĭ N., c1970: *Introductory real analysis*. Rev. English ed. translated and edited by Richard A. Silverman. Prentice-Hall,.

Stanford Vision Lab, Stanford University, Princeton University. ImageNet. Accesses October 29, 2019 http://www.image-net.org/

Iqbal, M. S., B. Luo, T. Khan, R. Mehmood, and M. Sadiq, 2018: Heterogeneous transfer learning techniques for machine learning. *Iran J Comput Sci*, **1**, 31–46, https://doi.org/10.1007/s42044-017-0004-z.

Kalogiros, J., and Q. Wang, 2011: Aircraft Observations of Sea-Surface Turbulent Fluxes Near the California Coast. *Boundary-Layer Meteorology*, **139**, 283–306, https://doi.org/10.1007/s10546-010-9585-x.

Krähenbühl, Philipp and Koltun, Vladlen, NIPS 2011: Efficient Inference in Fully Connected CRFs with Gaussian Edge Potentials, https://github.com/lucasb-eyer/pydensecrf

Monin, A. S., and A. M. Obukhov, 1954: Basic laws of turbulent mixing in the atmosphere near the ground. Tr. Akad. Nauk SSSR Geofiz. Inst., 24, 163–187.

National Centers for Environmental Prediction. Satellite Data Ingest at NCEP. Accessed August 31, 2019. https://www.emc.ncep.noaa.gov/mmb/data_processing/satellite_ingest.doc/document.htm

Obukhov, A. M., 1971: Turbulence in an atmosphere with a non-uniform temperature. *Boundary-Layer Meteorol*, **2**, 7–29, https://doi.org/10.1007/BF00718085.

Oliphant, T. E., 2007: Python for Scientific Computing. *Comput. Sci. Eng.*, **9**, 10–20, https://doi.org/10.1109/MCSE.2007.58.

Pagowski, M., and G. W. K. Moore, 2001: A Numerical Study of an Extreme Cold-Air Outbreak over the Labrador Sea: Sea Ice, Air–Sea Interaction, and Development of Polar Lows. *MONTHLY WEATHER REVIEW*, **129**, 26.

Petersen, G. N., and I. A. Renfrew, 2009: Aircraft-based observations of air–sea fluxes over Denmark Strait and the Irminger Sea during high wind speed conditions. *Quarterly Journal of the Royal Meteorological Society*, **135**, 2030–2045, https://doi.org/10.1002/qj.355.

Tetzlaff, A., C. Lüpkes, and J. Hartmann, 2015: Aircraft-based observations of atmospheric boundary-layer modification over Arctic leads: Boundary-Layer Modification Over Arctic Leads. *Q.J.R. Meteorol. Soc.*, **141**, 2839–2856, https://doi.org/10.1002/qj.2568.

Sandler, M., A. Howard, M. Zhu, A. Zhmoginov, and L.-C. Chen, 2019: MobileNetV2: Inverted Residuals and Linear Bottlenecks. *arXiv:1801.04381 [cs]*,.

Sea-mat/air-sea. Accessed March 4, 2019. https://github.com/sea-mat/air-sea

Sergeev, D., I. A. Renfrew, and T. Spengler, 2018: Modification of Polar Low Development by Orography and Sea Ice. *Mon. Wea. Rev.*, **146**, 3325–3341, https://doi.org/10.1175/MWR-D-18-0086.1.

Smith, S. D., 1988: Coefficients for sea surface wind stress, heat flux, and wind profiles as a function of wind speed and temperature. *J. of Geophys. Res.*, **93**, 15467, https://doi.org/10.1029/JC093iC12p15467.

Spengler, T., and Coauthors, 2016: High-Latitude Dynamics of Atmosphere–Ice–Ocean Interactions. *Bull. Amer. Meteor. Soc.*, **97**, ES179–ES182, https://doi.org/10.1175/BAMS-D-15-00302.1.

Stéfan van der Walt, Johannes L. Schönberger, Juan Nunez-Iglesias, François Boulogne, Joshua D. Warner, Neil Yager, Emmanuelle Gouillart, Tony Yu and the scikit-image contributors. scikit-image: Image processing in Python. PeerJ 2:e453 (2014) https://doi.org/10.7717/peerj.453

Tjernström, M., 2005: The Summer Arctic Boundary Layer during the Arctic Ocean Experiment 2001 (AOE-2001). *Boundary-Layer Meteorol*, **117**, 5–36, https://doi.org/10.1007/s10546-004-5641-8.

Vickers, D., L. Mahrt, and E. L. Andreas, 2013: Estimates of the 10-m Neutral Sea Surface Drag Coefficient from Aircraft Eddy-Covariance Measurements. *Journal of Physical Oceanography*, **43**, 301–310, https://doi.org/10.1175/JPO-D-12-0101.1.

U.S. National Ice Center, Naval Ice Center. NIC products. Accessed 10 May, 2019 https://www.natice.noaa.gov/Main_Products.htm.

U.S. Coast Guard, 2013: *Arctic Strategy*, U.S. Coast Guard Headquarters, 48 pp.

Zhang, X., J. Zou, K. He, and J. Sun, 2015: Accelerating Very Deep Convolutional Networks for Classification and Detection. *arXiv:1505.06798 [cs]*,.

THIS PAGE INTENTIONALLY LEFT BLANK

INITIAL DISTRIBUTION LIST

1. Defense Technical Information Center
   Ft. Belvoir, Virginia

2. Dudley Knox Library
   Naval Postgraduate School
   Monterey, California